Quantitative High-Resolution Sensing of DNA Hybridization Using Magnetic Tweezers with Evanescent Illumination

Electronic Supplementary Information

Piercen M. Oliver, Jin Seon Park, and Dmitri Vezenov

Lehigh University Chemistry, 6 E. Packer Ave., Bethlehem, PA 18015

S1. Electromagnet hysteresis. We took Hall sensor measurements of our electromagnet, while switching between 0 and 0.94 A of current in a sinusoidal fashion, at several different *total* cycle times (Figure S1). The data shows that essentially no hysteretic effects (<5 % maximum) due to induction were seen in our electromagnet with a *total* cycle time of 5 seconds or longer. All experiments described in the main text have a total cycle time of at least 6 seconds.

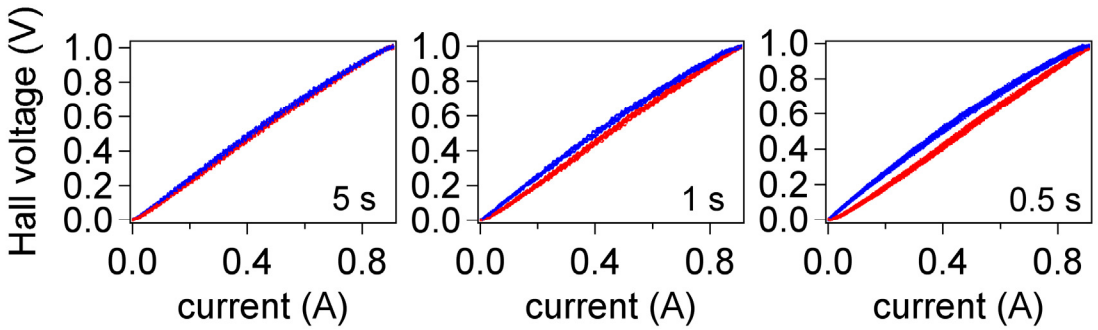

Figure S1: Hall sensor voltage (linearly proportional to magnetic field *B*) versus applied electromagnet current at three total cycle times relating to sinusoidal modulation of the electromagnet current. Both regions of increasing current (red) and decreasing current (blue) are plotted. At a 5 s cycle time, the hysteretic response essentially disappears.

S2. Probe Properties. A synthesis of force probes was developed to produce polymer microspheres with a range of compositions of nanoscopic or molecular inclusions (magnetic nanoparticles, quantum dots, or organic dyes) and resulted in a tight distribution of probe sizes. Our method, which uses controlled emulsification of polymer solutions, will be discussed elsewhere. The size distribution was derived by inspection of the SEM images of hundreds (300-600) of probes. A tight size distribution was established (Figure S2) from the images. All probes were uniformly spherical and their surfaces highly smooth.

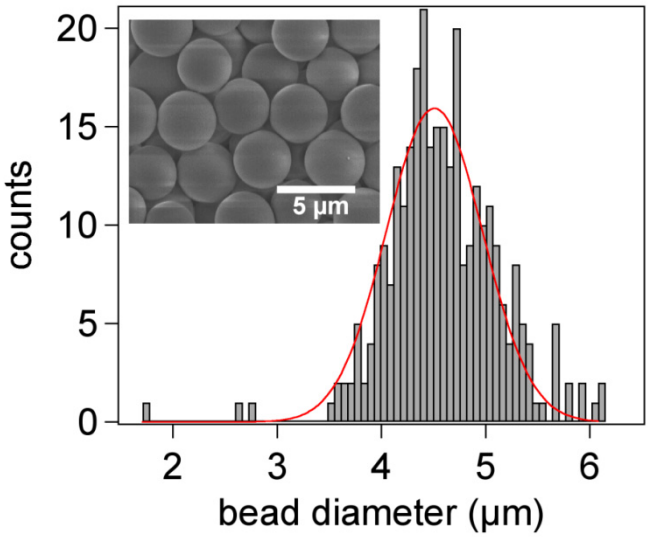

Figure S2: Histogram of diameters of synthesized beads. The probes contained both rhodamine 6G dye and magnetite nanoparticles (10 nm in diameter). Probe diameters were derived manually from SEM images over several hundred beads (inset). The histogram was fitted to a Gaussian and yielded a mean diameter of 4.51 μm and a standard deviation of 0.46 μm, which corresponds to a FWHM of 1.1 μm or ±12% of the mean.

Vibrating sample magnetometer (VSM) measurements showed that the probes were highly superparamagnetic — exhibiting no observable hysteresis (Figure S3 a). From Equation 2 in the main text, we were able to reconstruct the most likely relationship between force and applied field (Figure S3 b & c). The magnetic analysis is consistent with the fits to the FJC model of single DNA molecule under tension.

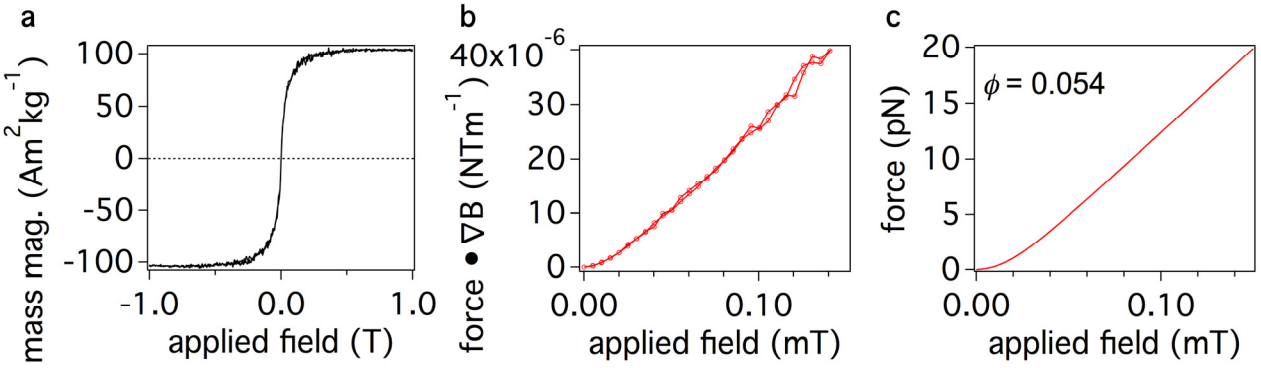

Figure S3: Magnetic properties of probes. (a) Vibrating sample magnetometer (VSM) measurement of mass magnetization vs. applied field. (b) Product of force and gradient of magnetic field versus applied field from combining Equation 2 in the main text with the VSM data (the exact magnetic field gradient is not known). Note the curvature at low field, which disappears after saturation. (c) Theoretical force versus field of one probe from Equation 2 in the text given a volume fraction for magnetite $\phi = 0.054$, a field gradient of 55 T m^{-1}, $D_{NP} = 10$ nm, $\rho_m = 5.046$ g cm^{-3}, $\rho_{bead} = 1.2$ g cm^{-3}, and a bead diameter of 4.5 μm.

S3. Evanescent field penetration depth from simultaneous atomic force microscopy (AFM)/TIRF measurement. The laser angle of incidence (TIRF angle) for the experiment detailed in the text was determined using a 45° glass (BK7) prism (data not shown). After force spectroscopy measurements, we conducted an AFM/TIRF experiment where a different probe was glued to an AFM cantilever (Figure S4) and imaged using the same 532 nm laser evanescent illumination as used in the text. Afterwards, due to differences in setup and alignment, the TIRF angle was measured again using the prism.

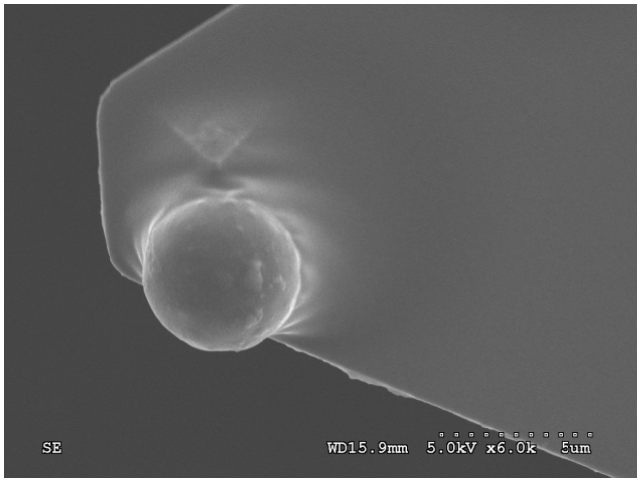

Figure S4: SEM image of a typical spherical force probe mounted on the AFM and used in the AFM/TIRF experiment to calibrate the decay length of fluorescent image intensity of these probes in the evanescent field.

The bead mounted on the AFM cantilever was moved in and out of contact with the surface for a total distance of 1 μm, while a movie of the probe's fluorescence was captured. Post-analysis was performed by averaging the retraction curves, normalizing to the maximum intensity (Figure S5 a), and retracing the data in terms of intensity versus distance (Figure S5 c). The distance was obtained by multiplying time scale by a known velocity of the AFM cantilever. The z position for contact was set to the distance at the onset of the linear compliance regime (Figure S5 b). Penetration depths were calculated using an exponential decay function with a z-offset (z_0):

$$I = I_0 \cdot \exp\left(-\frac{(z - z_0)}{d}\right) \tag{S1}$$

where I_0 is the intensity at contact (which should be close to 1, since the contact is assured when the AFM cantilever detects significant repulsive forces, Figure S5 b).

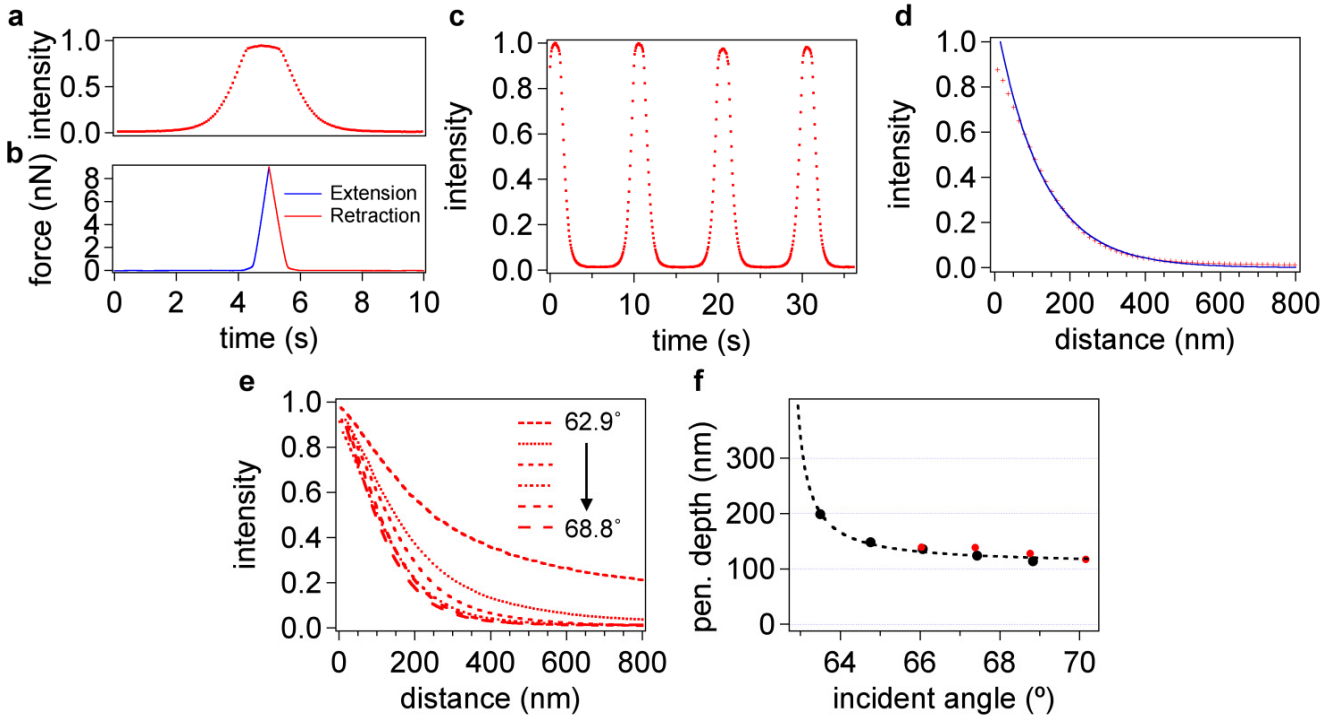

Figure S5: AFM/TIRF data and fitting results for determination of the evanescent field penetration depth. (a) Normalized intensity data for the extension and retraction of the probe/cantilever from the surface over a distance of 1 µm. (b) Force-time trace aligned with the intensity data in (a). (c) Intensity of the bead image in a series of approach-withdrawal curves. (d) An averaged retraction curve at one TIRF angle (red dots). The blue line indicates a fit to Equation S1, excluding distances below 20 nm, where observed repulsive forces (see part b, at time between 4.0 s and 4.3 s) move the probe away from the surface, thus, making actual separation underestimated. (e) Averaged data from several TIRF angles shifted using the offset from Equation S1. (f) Plot of penetration depth derived from fits from (e) (black dots) versus TIRF angle (dashed line is a guide to the eye). Red dots indicate penetration depths calculated from the fits in the main text (Table 1). Error bars are smaller than the markers.

We discovered that the intensity in the whole range of bead-surface distance could be defined as a single exponential decay reasonably well (Figure S5 d), excluding the region of repulsive forces where distance from surface is underestimated. The offset for the z-position, z_0, was generally small (0-9 nm), but helped overlay the averaged data in Figure S5 d, since the exact point of contact is not precisely known (due to repulsion near surface and possible roughness of the probe). The fitted maximum intensity did not differ from 1 by more than 0.06. As expected, an increase in the TIRF angle raises the penetration depth, which ranges between ~100 – 400 nm. Figure S5 f shows that the range of

penetration depth values from the fits to stretching model in the main text (red dots) are consistent with the AFM/TIRF data (black dots).

S4. Noise estimate from immobilized probes. An immobilized probe was imaged under several different instrumental conditions in order to determine the magnitude of fluctuations resulting from instrumental (thermal or mechanical, as well laser power, detector, shot, and electronic) noise. Although mechanical drift was low, a boxcar average of both the intensity and x-y fluctuations were taken in order to determine the average value (Figure S6). As expected, a decrease in exposure time and increase in gain raises both the intensity (i.e. z) and x-y noise. The intensity fluctuations in Figure S6 were used to subtract system noise from the z-variance in the force calculation below (Figure S9).

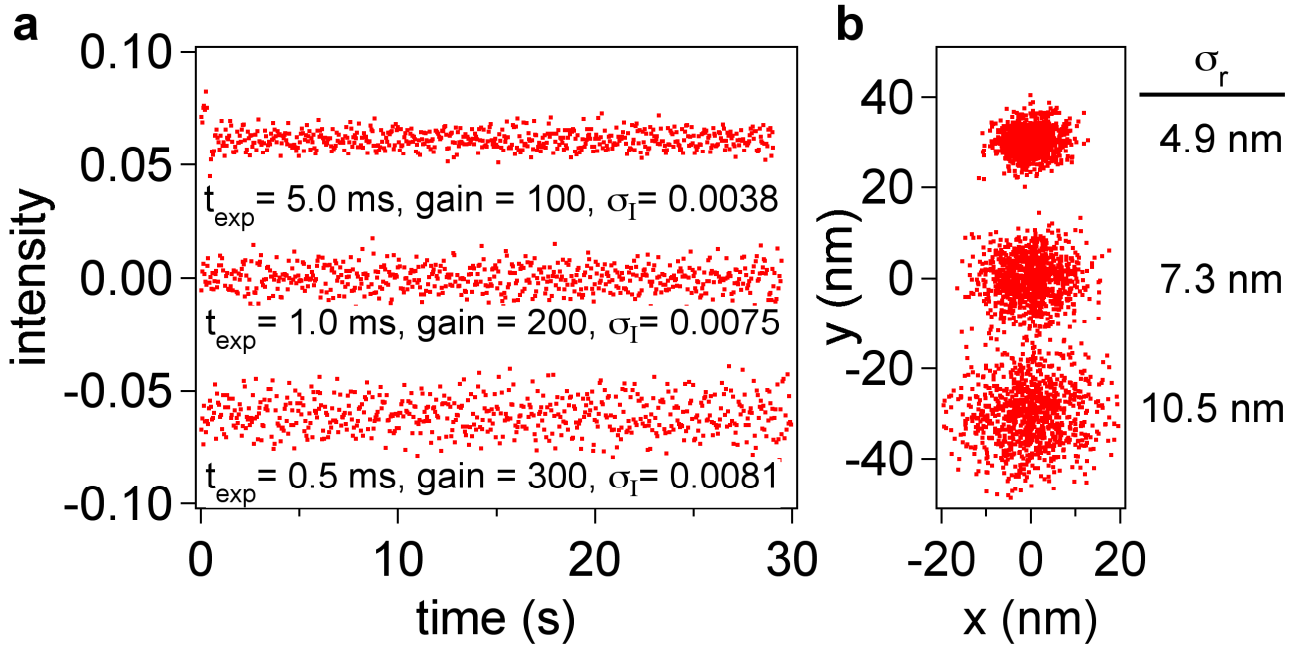

Figure S6: Noise of an immobilized bead under TIRF ($d \approx 140$ nm) at three different capture settings (t_{exp} is the exposure time, σ_I is the standard deviation in intensity from the normalized intensity of $I = 1$, and σ_r is the standard deviation of the lateral displacement from the averaged zero point). Mechanical drift was removed using a 50-point box filter and moving the average position of the center of the bead. (a) Intensity fluctuations (from the normalized initial intensity of $I = 1$) and (b) x-y positions are given. The x-y positions were determined from a 2-D Gaussian fit for each frame. As expected, a decrease in exposure time and increase in gain raises the noise level. The exposure time was not varied independently of the gain because the signal to noise ratio at low exposure times was poor (~ single digits). Given a penetration depth of $d \approx 140$ nm, the intensity-fluctuations σ_I correspond to σ_z = 0.53, 1.05, and 1.14 nm respectively. Since the probe is immobilized, the noise is purely instrument noise and is added to the variance of Brownian fluctuations of the tethered probe position. The electromagnet current was ramped during the capture of this data to ensure the probe was completely immobilized.

S5. Sample raw intensity-current data.

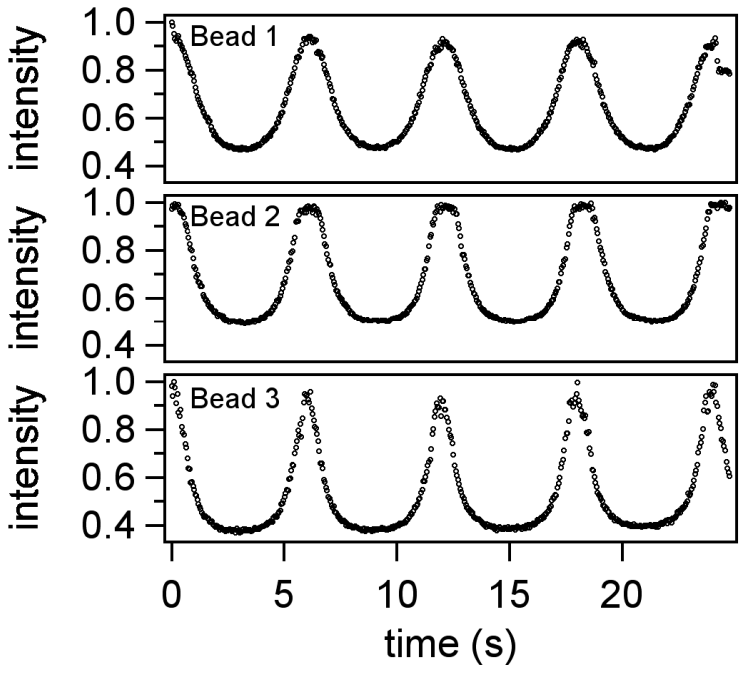

Figure S7: Examples of raw intensity-current curves captured from several other probes used in the experiment described in the main text.

S6. Converting intensity fluctuations to force. Intensity fluctuations of a probe in an evanescent field can be used to calculate the external force on a bead. The equipartition theorem relates tether stiffness, $\xi(z)$, to average z-variance $\left\langle \sigma_z^2 \right\rangle$,

$$\xi(z) = \frac{\mathrm{d}F}{\mathrm{d}z} = \frac{k_B T}{\left\langle \sigma_z^2 \right\rangle} \tag{S2}$$

which can be integrated as

$$F = k_B T \int_{z_0}^{z_1} \frac{dz}{\left\langle \sigma_z^2 \right\rangle}, \quad \text{or} \quad F(i) = k_B T \sum_{i_0}^{i} \frac{\Delta z_{avg}(i)}{\left(z_{avg}(i) - z(i)\right)^2} + C \tag{S3}$$

where i is the electromagnet current, z_{avg} is the averaged z-position, and Δz_{avg} is the change in the average position for an incremental change in current, and C is the constant of integration. For this type

of analysis, a great deal of points at a low exposure time must be taken. The exposure time must be short compared to the system's relaxation time τ_0,

$$\tau_0 = \frac{\gamma}{\xi(z)} \tag{S4}$$

where γ is the friction coefficient. For a sphere in water, $\gamma = 6\pi\eta r$, where η is the viscosity of water (0.001 Pa s for bulk) and r is the radius of the probe. Assuming a bead diameter of 4.5 μm and an elasticity of 2×10^{-4} N m^{-1} (200-mer ssDNA elasticity at ~75 nm extension), the correlated motion time is $\tau_0 = 0.2$ ms.

If a short exposure time is not possible (as in our case), some compensation for averaging of the probe movements during actual observation time (blurring) will have to be established. Blurring of the image causes the measured probe positions to be closer to one another than the true instantaneous positions at the same time intervals. In our case, an estimate for blurring effects can be made using a simple argument put forth by Towles, *et. al*.[1] The argument takes into account the apparent probe displacement distribution as a function of exposure time and probe friction coefficient. Although initially applied to *x*-*y* displacement, the argument should hold true for *z*-displacement as well. The actual fluctuations are corrected by a factor *S*,

$$\left\langle \sigma_z^2 \right\rangle_{\text{measured}} = S \cdot \left\langle \sigma_z^2 \right\rangle_{\text{actual}}, \quad \text{where} \quad S = \frac{\tau_0}{\delta t}\left[1 - \exp(\delta t / \tau_0)\right] \tag{S5}$$

where δt is the exposure time. Generally, *S* becomes a function of stiffness (Equation S4), which varies with extension and applied force. For a 200-mer single stranded DNA, the stiffness can be derived from analysis of the relationship in Equation 5 of the text. Diffusion near the surface is hindered and, consequently, effective viscosity in the z-direction raises the relaxation time.[2, 3] This effective viscosity in the z-direction is given as:

$$\eta^* = \left(1 + \frac{r}{z} + \frac{r}{6z + 2r}\right) \cdot \eta \tag{S6}$$

Plots of the theoretical correction factor using bulk and effective viscosities are displayed in Figure S8 for several different exposure times for a 4.5 μm diameter probe. For exposure times of a few ms typical

of our experimental setup, the blurring correction can be anywhere between 5-10 % and an order of magnitude effect, depending on the contribution from hindered diffusion.

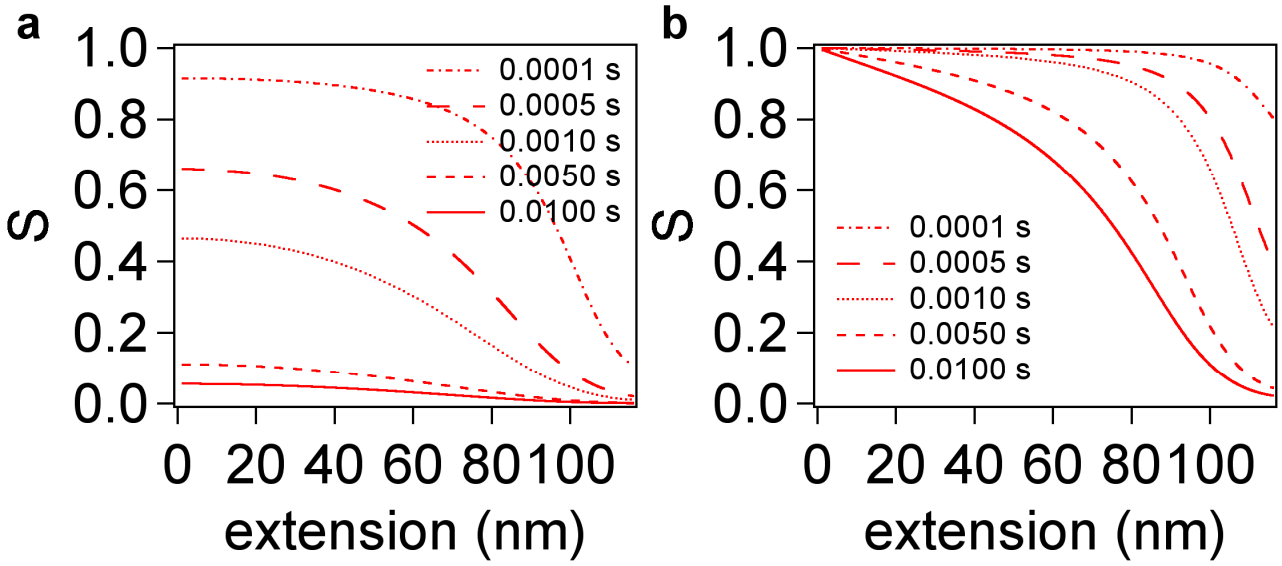

Figure S8: Correction factor (*S*-value in Equation S5) for measured z variance versus extension for a 4.5 μm diameter probe tethered to a 200-mer ssDNA (a) using the bulk viscosity value and (b) correcting for hindered diffusion using Equation S6. At decreased exposure times, the correction approaches unity. The decrease in *S*-value at higher extensions is due to the increase in tether stiffness and shortening of the characteristic time scale (Equation S5).

The basic method for obtaining fluctuations proceeds as follows (Figure S9): (i) determine intensity fluctuations at a low exposure time while slowly ramping the current linearly, (ii) calculate the residuals against an averaged curve (model fit), (iii) convert the residuals to z-displacement based on a known penetration depth, (iv) bin the values of z-displacement as a function of extension to obtain an estimate of z-variance, (v) subtract instrumental noise, and (vi) integrate the result according to Equation S3 and fit the low-extension region to a line in order to determine the constant of integration *C*. The fluctuation curves in Figure S9 are obtained from extension traces; the contour length derived from the fits in Figure S9 consistently indicated a ssDNA contour length of ~99 nm, or ~170 bases. The reduction in the overall contour length in the extension traces (from an expected 200 bases) likely comes from formation of marginally stable hairpins.

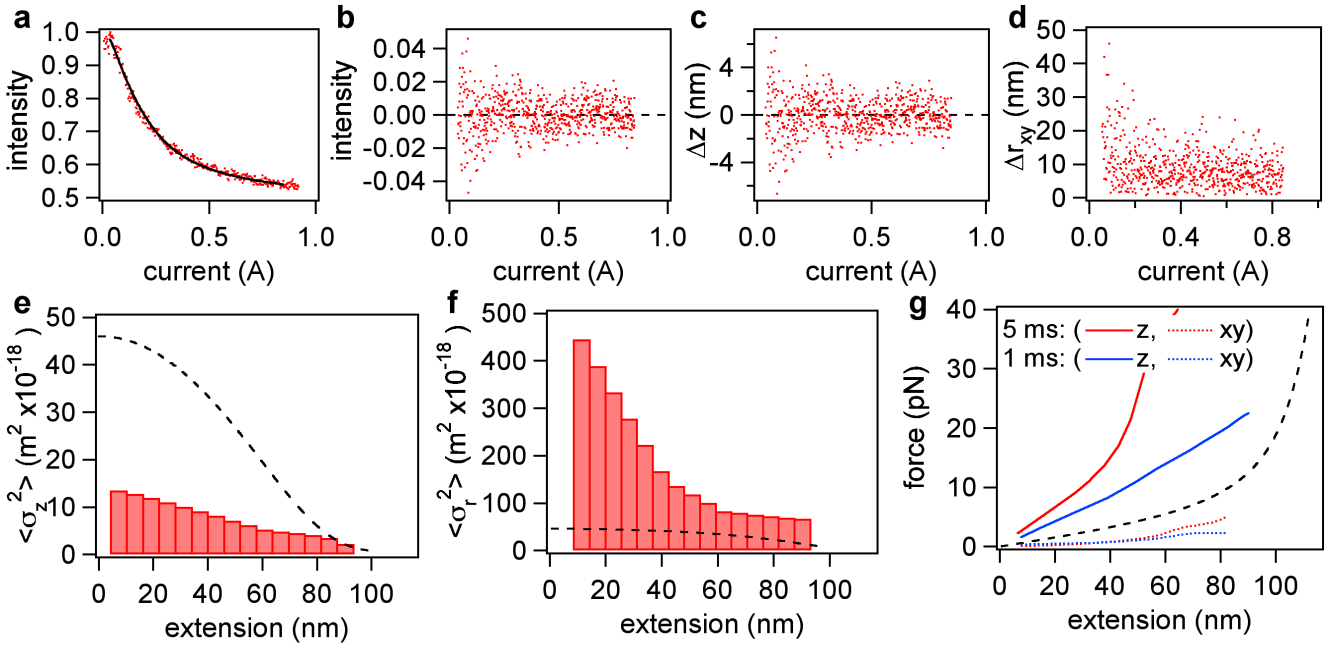

Figure S9: Method for obtaining forces from intensity and xy fluctuations. (a) Intensity versus electromagnet current (red) for an extension ramp at 0.05 Hz (δt = 5 ms, camera gain = 100). The black line is a fit to Equation (6) in the main text used to determine the intensity at a particular current. All fits consistently yielded a contour length of ~99 nm, presumably due to secondary structure seen in extension curves. (b) Residuals against the fitted curve as a function of current. (c) Intensity fluctuations converted to z-displacements from a known penetration depth (d = 139 nm) as a function of current. (d) x-y displacement fluctuations (depicted as fluctuation in radius-vector $\Delta r_{xy} = \sqrt{\sigma_x^2 + \sigma_y^2}$ as a function of current. Sample drift was calculated by box filtering x and y data. The drift was subtracted from the raw x and y data in order to calculate r-displacements. (e) Binned z-variance as a function of extension along with the expected theoretical variance (dashed line) for a 170-mer. (f) Binned xy-variance as a function of extension with theoretical variance (dashed line) for a 170-mer. (g) Force versus extension for z and xy fluctuations at two exposure times, 5 and 1 ms, along with theory (dashed line) for a 170-mer. The constant of integration C is determined by fitting a line to data from the 5 – 20 nm extension region (black dotted line). Extension was obtained from intensity data and independently known penetration depth.

As evident from Figure S9 d, use of fluctuations in the bead position to calculate forces acting on tethered DNA molecule reproduces predicted trends: in both cases, we observe increased force with a longer extension. This method, however, yields forces that are approximately within a factor of two to three from the values determined using fits to stretching models described in the main text. Use of z-fluctuations (Equation S1) overestimated the forces due to blurring effect described above, whereas the use of lateral fluctuations underestimated the forces, because measurements of lateral positions are not differential (unlike z-position, which is referenced to the solid-liquid interface due to the nature of the evanescent field), therefore, other sources of noise could contribute significantly to the observed x-y plane fluctuations of these short tethers. Since our ultimate goal is to carry out parallel force spectroscopy with continuous rapid force-curve acquisition, data capture with CCD camera is the

natural choice for this approach and compatible with the calibration of the system using equation of state for a macromolecule. Use of fluctuations would require significant changes to hardware setup, making data capture and analysis substantially more complicated than in the first case.

References

1. Towles, K. B.; Beausang, J. F.; Garcia, H. G.; Phillips, R.; Nelson, P. C., *Phys. Biol.* **2009,** *6*, 025001.
2. Bevan, M.; Prieve, D., *The Journal of Chemical Physics* **2000,** *113*, 1228-1236.
3. Kruithof, M.; Chien, F.; De Jager, M.; Van Noort, J., *Biophys. J.* **2008,** *94*, 2343-2348.